Solution of Fluid-Structure Interaction Problems using a Discontinuous Galerkin Technique

by

Anshul Mohnot

Submitted to the Computation for Design and Optimization
in partial fulfillment of the requirements for the degree of

Master of Science in Computation for Design and Optimization

at the

MASSACHUSETTS INSTITUTE OF TECHNOLOGY

May 2008

Author .....
Computation for Design and Optimization
May 16, 2008

Certified by .....
Jaime Peraire
Professor, Department of Aeronautics and Astronautics
Thesis Supervisor

Accepted by .....
Jaime Peraire
Director, Computation for Design and Optimization

Solution of Fluid-Structure Interaction Problems using a Discontinuous Galerkin Technique

by

Anshul Mohnot

Submitted to the Computation for Design and Optimization
on May 16, 2008, in partial fulfillment of the
requirements for the degree of
Master of Science in Computation for Design and Optimization

Abstract

The present work aims to address the problem of fluid-structure interaction using a discontinuous Galerkin approach. Starting from the Navier-Stokes equations on a fixed domain, an arbitrary Lagrangian Eulerian (ALE) approach is used to derive the equations for the deforming domain. A geometric conservation law (GCL) is then introduced, which guarantees freestream preservation of the numerical scheme. The space discretization is performed using a discontinuous Galerkin method and time integration is performed using either an explicit four stage Runge-Kutta scheme or an implicit BDF2 scheme. The mapping parameters for the ALE formulation are then obtained using algorithms based on radial basis functions (RBF) or linear elasticity. These strategies are robust and can be applied to bodies with arbitrary shapes and undergoing arbitrary motions. The robustnesss and accuracy of the ALE scheme coupled with these mapping strategies is then demonstrated by solving some model problems. The ability of the scheme to handle complex flow problems is demonstrated by analyzing the low Reynolds number flow over an oscillating circular cylinder.

Thesis Supervisor: Jaime Peraire
Title: Professor, Department of Aeronautics and Astronautics

Acknowledgments

First and Foremost, I would like to thank my advisor Professor Jaime Peraire for his guidance, support and encouragement throughout my stay at MIT.

Also, I would like to thank Dr. Per-Olof Persson for his help and suggestions with the formulation and debugging, and Dr. David Willis for his help on identifying potential test problems.

Also, I would like to thank Ms. Laura Koller for all her help, reminder emails, and the good food. Also, I would like to thank Ms. Jean Sofranos for helping me in locating Jaime.

I would like to thank my parents for their support, encouragement and seek their blessings. I would like to thank all my friends for making my stay at MIT a wonderful experience. Finally, I would like to thank Arpita for making my stay at MIT, the most memorable one.

Contents

List of Figures

List of Tables

Chapter 1

Introduction

There is a growing interest in high-order numerical methods, such as discontinuous Galerkin (DG), for fluid problems mainly because of their capability to produce highly accurate solutions with minimum numerical dissipation. An important area for such methods is problems involving time-varying geometries such as rotor-stator interactions, flapping flight or fluid-structure interactions.

One of the approaches to solve problems involving moving geometries is to find a time-varying mapping between the fixed reference domain and the physical time-varying domain. The original conservation law is then transformed using this mapping to the reference configuration, which is then solved using a high-order scheme. In this method, the actual computation is carried out on a fixed mesh and the variable domain geometry is accounted for through a modification of the fluxes in the conservation law. This approach is simple and allows for arbitrarily high-order solutions of the Navier-Stokes equations.

Ref. [1] describes a methodology to perform the above mentioned transformations. Figure 1, taken from [1], shows a solution of the compressible Navier-Stokes equations on a deformable mesh. The front cylinder oscillates thus creating a strong vortex street which interacts with an oscillating plunging and pitching airfoil. For appropriate distances between the two objects, substantial thrust can be produced on the foil. The plot shows the mesh used and the vorticity distribution. The mapping parameters in this example are obtained using an explicit algebraic blending

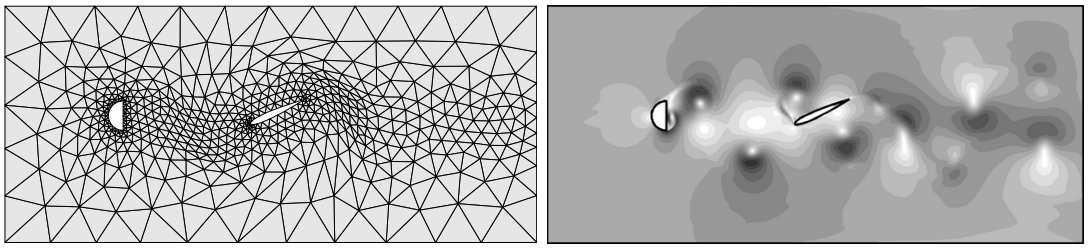

(a) Deformed mesh (b) Vorticity

Figure 1-1: Cylinder and foil oscillating in a viscous fluid, with thrust being generated at the foil.

approach. This method though easy to implement, cannot be extended to arbitrary movements of the boundaries and geometries. Hence a robust strategy to obtain the mapping parameters is required.

The problem of obtaining the mapping parameters is similar to the problem of mesh movement. Ref. [2] gives an overview of commonly used unstructured mesh movement strategies. In the present work, we study approaches based on radial basis functions (Refs. [3], [4]) and linear elasticity (Refs. [2], [5], [6], [7], [8]).

The radial basis function based approach is a multivariate interpolation scheme and is commonly used in fluid-structure interaction problems to transfer information between the structural and the aerodynamic mesh[9]. This method requires no grid connectivity, which makes it very attractive for unstructured mesh movement applications.

In the linear elasticity approach, the space occupied by the mesh is assumed to be an elastic medium which deforms according to the linear elasticity equations. The elasticity equations are then discretized using the existing mesh and displacements are calculated at the nodes. To obtain additional grid control, body forces can be added. We note that in a time varying setting the elasticity equations are non-dissipative and hence waves generated during the motion are not damped and stay in the computational domain. To remedy this situation we incorporate a dissipative linear viscoelastic model which has the desired effect of attenuating the waves over time.

The objective of this work is to investigate various approaches to obtain the map-

ping parameters for the ALE approach. The ALE approach, along with the modified Navier-Stokes equations and the geometric conservation law (GCL) are discussed in chapter 2. Chapter 3 contains the details on obtaining the mapping parameters using the radial basis function and linear elasticity approaches.

In chapter 4, we solve the flow equations with these mapping techniques and present results demonstrating high-order accuracy and robustness of these schemes. We also present a coupled ALE-linear elasticity formulation, in which the equations for the flow and mesh movement are solved simultaneously.

Finally, to demonstrate the capability to solve real problems, we obtain solutions for flow over an oscillating cylinder for various low Reynolds number flow regimes.

Chapter 2

Governing Equations

In the chapter, governing equations for two dimensional unsteady flow on a deformable domain are presented. Starting from the Navier-Stokes equations on a fixed domain, an arbitrary Lagrangian Eulerian (ALE) approach is used to derive the equations on the deformable domain. The modified equations are always solved on the reference domain which is fixed in space and time. The solution of these transformed equations on the reference domain fails to exactly preserve the freestream solution. This situation is remedied by introducing an additional equation or the so called, geometric conservation law (GCL). The transformed Navier-Stokes equations along with GCL, are discretized on an unstructured triangular reference grid using the discontinuous Galerkin technique. Time integration is performed using either an explicit four stage Runge-Kutta method or an implicit BDF scheme.

2.1 Navier-Stokes Equations on a Deformable Domain

The Navier-Stokes equations in the physical domain $(\boldsymbol{x}, t)$ can be written in an integral form as,

$$\int_{v(t)} \frac{\partial \boldsymbol{U}}{\partial t}\, dv + \int_{\partial v} \boldsymbol{F} \cdot n\, da = 0, \tag{2.1}$$

where $v(t)$ is the control volume with boundary ∂v, n is the outward unit normal in $v(t)$, $\boldsymbol{U}$ is the vector of conserved variables and $\boldsymbol{F}$ are the corresponding fluxes in each of the spatial coordinate directions. Here, $\boldsymbol{F}$ incorporates both inviscid and viscous contributions, i.e., $\boldsymbol{F} = \boldsymbol{F}^{inv}(\boldsymbol{U}) + \boldsymbol{F}^{vis}(\boldsymbol{U}, \boldsymbol{\nabla U})$, where $\boldsymbol{\nabla}$ represents the spatial gradient operator in the $\boldsymbol{x}$ variables. The detailed expressions for the vector $\boldsymbol{U}$ and the fluxes $\boldsymbol{F}$ are given in appendix A.

In the following sections, we transform the Navier-Stokes equations to a fixed reference domain. This derivation is taken from reference [1] and is presented here for completeness.

2.1.1 Preliminaries

Given the physical domain, $v(t)$, we introduce an arbitrary reference domain V and a time dependent one-to-one mapping $\mathcal{G}(\boldsymbol{X}, t)$ between V and $v(t)$ as shown in figure 2-1. Thus, a point $\boldsymbol{X}$ in V is uniquely mapped to a point $\boldsymbol{x}(t)$ in $v(t)$, which is given by $\boldsymbol{x}(t) = \mathcal{G}(\boldsymbol{X}, t)$. Next, we introduce, the mapping deformation gradient $\boldsymbol{G}$, mapping velocity $\boldsymbol{v}_X$ and the jacobian of the mapping as,

$$\boldsymbol{G} = \boldsymbol{\nabla}_{\boldsymbol{X}}\mathcal{G}, \qquad \boldsymbol{v}_X = \left.\frac{\partial \mathcal{G}}{\partial t}\right|_X, \qquad g = \det(\boldsymbol{G}). \tag{2.2}$$

Let $d\boldsymbol{A} = \boldsymbol{N}dA$ denote an area element which after deformation becomes $d\boldsymbol{a} = \boldsymbol{n}da$, where $\boldsymbol{N}$ and $\boldsymbol{n}$ are the outward unit normals in V and $v(t)$, respectively. We note that the infinitesimal vectors $d\boldsymbol{L}$ in V and $d\boldsymbol{l}$ in $v(t)$ are related as $d\boldsymbol{l} = \boldsymbol{G}d\boldsymbol{L}$ and the corresponding elemental volumes, $dV = d\boldsymbol{L} \cdot d\boldsymbol{A}$ and $dv = d\boldsymbol{l} \cdot d\boldsymbol{a}$, are related as $dv = gdV$. Therefore, we must have

$$\boldsymbol{n}\, da = g\boldsymbol{G}^{-T}\boldsymbol{N}dA, \qquad \text{and} \qquad \boldsymbol{N}\, dA = g^{-1}\boldsymbol{G}^{T}\boldsymbol{n}\, da. \tag{2.3}$$

2.1.2 Transformed Equations

To obtain the Navier-Stokes equations in the reference domain, we start with the integral form of the equations (refer equation 2.1) and utilize the mapping to transform

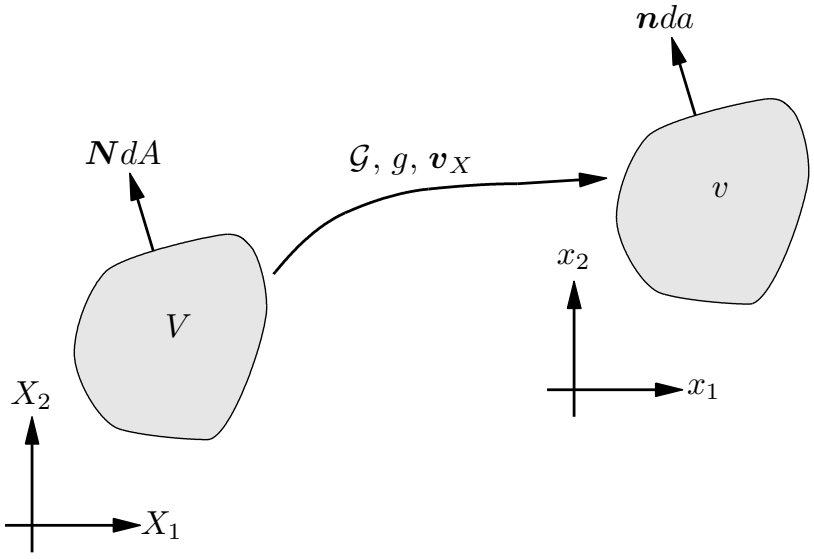

Figure 2-1: Mapping between the physical and the reference domains.

these integrals to the reference domain. Consider first the second term,

$$\int_{\partial v} \boldsymbol{F} \cdot \boldsymbol{n}\, da = \int_{\partial V} \boldsymbol{F} \cdot (g\boldsymbol{G}^{-T}\boldsymbol{N})\, dA = \int_{\partial V} (g\boldsymbol{G}^{-1}\boldsymbol{F}) \cdot \boldsymbol{N}\, dA, \tag{2.4}$$

similarly, using the Reynolds transport theorem the first integral can be transformed as,

$$\begin{aligned} \int_{v(t)} \frac{\partial \boldsymbol{U}}{\partial t}\, dv &= \frac{d}{dt}\int_{v(t)} \boldsymbol{U}\, dv - \int_{\partial v} (\boldsymbol{U}\boldsymbol{v}_X) \cdot \boldsymbol{n}\, da \\ &= \frac{d}{dt}\int_V g^{-1}\boldsymbol{U}\, dV - \int_{\partial V} (\boldsymbol{U}\boldsymbol{v}_X) \cdot (g\boldsymbol{G}^{-T}\boldsymbol{N})\, dA \\ &= \int_V \left.\frac{\partial (g^{-1}\boldsymbol{U})}{\partial t}\right|_X dV - \int_{\partial V} (g\boldsymbol{U}\boldsymbol{G}^{-1}\boldsymbol{v}_X) \cdot \boldsymbol{N}\, dA. \end{aligned} \tag{2.5}$$

Combining the expressions from equations 2.4 and 2.5, we obtain,

$$\int_V \left.\frac{\partial (g^{-1}\boldsymbol{U})}{\partial t}\right|_X dV + \int_{\partial V} (g\boldsymbol{G}^{-1}\boldsymbol{F} - g\boldsymbol{U}\boldsymbol{G}^{-1}\boldsymbol{v}_X) \cdot \boldsymbol{N}\, dA. \tag{2.6}$$

Using the divergence theorem we obtain a local conservation law in the reference domain as,

$$\left.\frac{\partial \boldsymbol{U}_X}{\partial t}\right|_X + \boldsymbol{\nabla}_X \cdot \boldsymbol{F}_X(\boldsymbol{U}_X, \boldsymbol{\nabla}_X \boldsymbol{U}_X) = 0, \tag{2.7}$$

where the time derivative is at a constant $\boldsymbol{X}$ and the spatial derivatives are taken with respect to the $\boldsymbol{X}$ variables. The transformed vector of conserved quantities and corresponding fluxes in the reference space are,

$$\boldsymbol{U}_X = g\boldsymbol{U} \ , \qquad \boldsymbol{F}_X = g\boldsymbol{G}^{-1}\boldsymbol{F} - \boldsymbol{U}_X\boldsymbol{G}^{-1}\boldsymbol{v}_X, \tag{2.8}$$

or, more explicitly,

$$\boldsymbol{F}_X = \boldsymbol{F}_X^{inv} + \boldsymbol{F}_X^{vis} \ , \qquad \boldsymbol{F}_X^{inv} = g\boldsymbol{G}^{-1}\boldsymbol{F}^{inv} - \boldsymbol{U}_X\boldsymbol{G}^{-1}\boldsymbol{v}_X \ , \qquad \boldsymbol{F}_X^{vis} = g\boldsymbol{G}^{-1}\boldsymbol{F}^{vis} \ , \tag{2.9}$$

and by simple chain rule,

$$\boldsymbol{\nabla U} = \boldsymbol{\nabla}_X(g^{-1}\boldsymbol{U}_X)\boldsymbol{G}^{-T} = (g^{-1}\boldsymbol{\nabla}_X\boldsymbol{U}_X - \boldsymbol{U}_X\boldsymbol{\nabla}_X(g^{-1}))\boldsymbol{G}^{-T} \ . \tag{2.10}$$

2.2 Geometric Conservation Law

The solution of the transformed equations in the reference domain results in non-preservation of uniform flow because of inexact integration of the jacobian. To achieve the preservation of uniform flow, a geometric conservation law (GCL)[10], is introduced and solved with the flow equations. To derive the GCL, we first obtain the so-called Piola relationships for arbitrary vectors $\boldsymbol{W}$ and $\boldsymbol{w}$, using equation 2.3 and the divergence theorem,

$$\boldsymbol{\nabla}_X \cdot \boldsymbol{W} = g\boldsymbol{\nabla} \cdot (g^{-1}\boldsymbol{G}\boldsymbol{W}) \ , \qquad \boldsymbol{\nabla w} = g^{-1}\boldsymbol{\nabla}_X \cdot (g\boldsymbol{G}^{-1}\boldsymbol{w}). \tag{2.11}$$

When the solution $\boldsymbol{U}$ is constant, say $\bar{\boldsymbol{U}}$, we have

$$\boldsymbol{\nabla}_X \cdot \boldsymbol{F}_X = g\boldsymbol{\nabla} \cdot (\boldsymbol{F} - \bar{\boldsymbol{U}}\boldsymbol{v}_X) = -g\bar{\boldsymbol{U}}\boldsymbol{\nabla} \cdot \boldsymbol{v}_X = -[\boldsymbol{\nabla}_X \cdot (g\boldsymbol{G}^{-1}\boldsymbol{v}_X)]\bar{\boldsymbol{U}}.$$

Therefore, for a constant solution $\bar{\boldsymbol{U}}$, equation (2.7) becomes

$$\left.\frac{\partial \boldsymbol{U}_X}{\partial t}\right|_X + \boldsymbol{\nabla}_X \cdot \boldsymbol{F}_X = \bar{\boldsymbol{U}}_x \left(\left.\frac{\partial g}{\partial t}\right|_X - \boldsymbol{\nabla}_X \cdot (g\boldsymbol{G}^{-1}\boldsymbol{v}_X) \right) \ .$$

We see that the right hand side is only zero if the equation for the time evolution of the transformation Jacobian g

$$\left.\frac{\partial g}{\partial t}\right|_X - \boldsymbol{\nabla}_X \cdot (g\boldsymbol{G}^{-1}\boldsymbol{v}_X) = 0 \ ,$$

is integrated exactly by our numerical scheme. Since in general, this will not be the case, the constant solution $\bar{\boldsymbol{U}}_x$ in the physical space will not be preserved exactly. Following [1], the system of conservation laws (2.7) is replaced by

$$\left.\frac{\partial (\bar{g} g^{-1} \boldsymbol{U}_X)}{\partial t}\right|_X + \boldsymbol{\nabla}_X \cdot \boldsymbol{F}_X = \boldsymbol{0}, \tag{2.12}$$

where $\bar{g}$ is obtained by solving the following equation using the same numerical time integration scheme as for the remaining equations

$$\left.\frac{\partial \bar{g}}{\partial t}\right|_X - \boldsymbol{\nabla}_X \cdot (g\boldsymbol{G}^{-1}\boldsymbol{v}_X) = 0 \ . \tag{2.13}$$

2.3 DG Formulation

In order to develop a discontinuous Galerkin method, we rewrite the above equations as a system of first order equations,

$$\left.\frac{\partial \boldsymbol{U}_X}{\partial t}\right|_X + \boldsymbol{\nabla}_X \cdot \boldsymbol{F}_X(\boldsymbol{U}_X, \boldsymbol{Q}_X) = 0, \tag{2.14}$$

$$\boldsymbol{Q}_X - \boldsymbol{\nabla}_X U_X = 0. \tag{2.15}$$

Next, we introduce the '*broken*' DG spaces $\mathcal{V}^h$ and Σ^h associated with the triangulation $\mathcal{T}^h = \{K\}$ of V. In particular, $\mathcal{V}^h$ and Σ^h denote the spaces of functions whose restriction to each element K are polynomials of order $p \geq 1$.

Following [11], we consider DG formulations of the form: find $\boldsymbol{U}_X^h \in \mathcal{V}^h$ and

$\boldsymbol{Q}_X^h \in \Sigma^h$ such that for all $K \in \mathcal{T}^h$, we have

$$\int_K \left.\frac{\partial \boldsymbol{U}_X^h}{\partial t}\right|_X \boldsymbol{V}\, dV - \int_K \boldsymbol{F}_X(\boldsymbol{U}_X^h, \boldsymbol{Q}_X^h) \cdot \boldsymbol{\nabla}_X \boldsymbol{V}\, dV - \int_{\partial K} \boldsymbol{V}(\hat{\boldsymbol{F}}_X \cdot \boldsymbol{N})\, dA = 0 \qquad \forall \boldsymbol{V} \in \mathcal{V}^h, \tag{2.16}$$

$$\int_K \boldsymbol{Q}_X^h \boldsymbol{P}\, dV + \int_K \boldsymbol{U}_X^h \boldsymbol{\nabla}_X \cdot \boldsymbol{V}\, dV - \int_{\partial K} \hat{\boldsymbol{U}}_X^h(\boldsymbol{P} \cdot \boldsymbol{N})\, dA = 0 \qquad \forall \boldsymbol{P} \in \Sigma^h. \tag{2.17}$$

Here, the numerical fluxes $\hat{\boldsymbol{F}}_X \cdot \boldsymbol{N}$ and $\hat{\boldsymbol{U}}_X$ are approximations to $\boldsymbol{F}_X \cdot \boldsymbol{N}$ and to $\boldsymbol{U}_X$, respectively, on the boundary of the element K. The DG formulation is complete once we specify the numerical fluxes $\hat{\boldsymbol{F}}_X \cdot \boldsymbol{N}$ and $\hat{\boldsymbol{U}}_X$ in terms of $(\boldsymbol{U}_X^h)$ and $(\boldsymbol{Q}_X^h)$ and the boundary conditions. The flux term $\hat{\boldsymbol{F}}_X \cdot \boldsymbol{N}$ is decomposed into its inviscid and viscous parts,

$$\hat{\boldsymbol{F}}_X \cdot \boldsymbol{N} = \hat{\boldsymbol{F}}_N^{\text{inv}}(\boldsymbol{U}_X^h) + \hat{\boldsymbol{F}}_N^{\text{vis}}(\boldsymbol{U}_X^h, \boldsymbol{Q}_X^h). \tag{2.18}$$

The numerical fluxes $\hat{\boldsymbol{F}}_N^{\text{vis}}$ and $\hat{\boldsymbol{U}}_X$ are chosen according to the compact discontinuous Galerkin (CDG) method [12]. This is a variant of the local discontinuous Galerkin (LDG) method[11], but has the advantage of being compact on general unstructured meshes.

The inviscid numerical flux $\hat{\boldsymbol{F}}_N^{\text{inv}}(\boldsymbol{U}_X^h)$ is chosen according to the method proposed by Roe [13]. Note that this flux can be very easily derived from the standard Eulerian Roe fluxes by noting that the flux $\boldsymbol{F}_X^{inv} \cdot \boldsymbol{N}$ can be written as

$$\boldsymbol{F}_X^{inv} \cdot \boldsymbol{N} = (\boldsymbol{F}^{inv} - \boldsymbol{U}\boldsymbol{v}_X) \cdot g\boldsymbol{G}^{-T}\boldsymbol{N}\ ,$$

where $g\boldsymbol{G}^{-T}\boldsymbol{N}$ (from (2.3)) is always continuous across the interface (assuming that $\mathcal{G}$ is continuous), and the eigenvalues and eigenvectors of the Jacobian matrix for $\boldsymbol{F} - \boldsymbol{U}\boldsymbol{v}_X$ are trivially obtained from the Jacobian matrix for the standard Eulerian flux $\boldsymbol{F}$.

For the GCL, the inter-element fluxes can be evaluated with little overhead, as the fluxes depend only on the mapping (assumed to be continuous) and no additional information is required from the neighbouring elements.

2.4 Time Integration

The DG discretization yields a system of ordinary differential equations of the form,

$$\frac{\partial \boldsymbol{U}}{\partial t} = \boldsymbol{R}(t, \boldsymbol{U}(t)), \tag{2.19}$$

where $\boldsymbol{R}$ is the residual computed at each time step. The time integration of the ODE is performed using either an explicit four stage Runge-Kutta method or an implicit BDF2 method as described below.

Four Stage Runge-Kutta Method

The explicit four stage Runge-Kutta method is given by,

$$\boldsymbol{U}^{t+1} = \boldsymbol{U}^{t} + \frac{\Delta t}{6}\left(k_1 + 2k_2 + 2k_3 + k_4\right), \tag{2.20}$$

where

$$\begin{aligned}
k_1 &= \boldsymbol{R}\left(t_n, \boldsymbol{U}_n\right), \\
k_2 &= \boldsymbol{R}\left(t_n + \frac{\Delta t}{2}, \boldsymbol{U}_n + \frac{k_1}{2}\right), \\
k_3 &= \boldsymbol{R}\left(t_n + \frac{\Delta t}{2}, \boldsymbol{U}_n + \frac{k_2}{2}\right), \\
k_4 &= \boldsymbol{R}\left(t_n + \Delta t, \boldsymbol{U}_n + k_3\right).
\end{aligned}$$

BDF2 Method

The BDF2 method is an implicit linear two-step method and can be written as,

$$\boldsymbol{U}^{t+1} = -\frac{1}{3}\boldsymbol{U}^{t-1} + \frac{4}{3}\boldsymbol{U}^{t} + \frac{2\Delta t}{3}\boldsymbol{R}. \tag{2.21}$$

First-order implicit Euler can be used for the first time step. The main advantage of BDF2 over other implicit schemes is that it requires only one nonlinear solve at each time step.

Chapter 3

Mapping Techniques

3.1 Introduction

In this chapter, we introduce various mapping approaches to compute the mesh velocities and deformation gradients required for the ALE computations. The methods presented in literature are primarily algebraic, (spring analogy[14] or interpolation based), or PDE based approaches.

In the present work, we explore three approaches, two are algebraic in nature and are based on interpolation methods, and one is a PDE based approach where the mesh movement is achieved by solving linear elastodynamics equations.

3.2 Blending Function Approach

The blending function approach[1], uses odd degree polynomial blending functions to obtain explicit expressions for the mappings. These polynomials, $r_n(x)$, satisfy $r(0) = 0$, $r(1) = 1$ and have $(n-1)/2$ vanishing derivatives at $x = 0$ and $x = 1$.
An example taken from reference [1], shows a square domain with a rectangular hole deformed such that the hole is displaced and rotated but the outer boundary is fixed.

The mapping is defined by introducing a circle C centered at $\boldsymbol{X}_C$ with a radius R_C that contains the moving boundary. The distance from a point $\boldsymbol{X}$ to C is then $d(\boldsymbol{X}) = \|\boldsymbol{X} - \boldsymbol{X}_C\| - R_C$, where $\|\cdot\|$ is the Euclidean length function. The blending

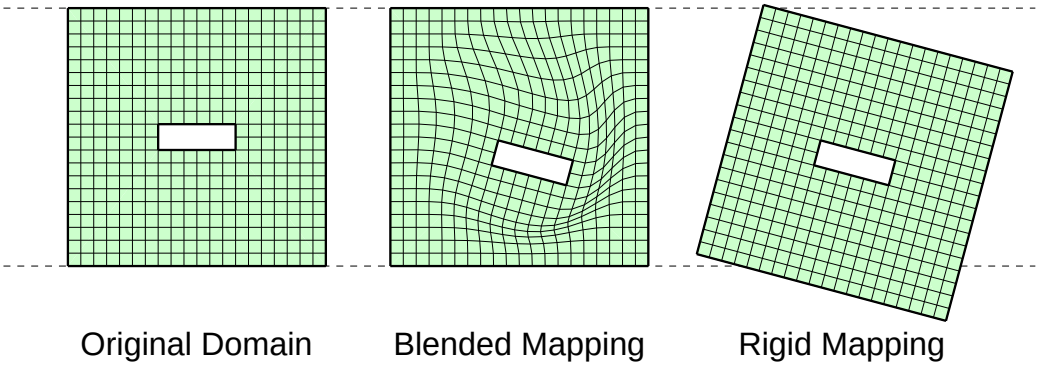

Figure 3-1: Deformation by blending of the original domain and a rigidly displaced domain.

function in terms of the distance $d(\boldsymbol{X})$ is given by,

$$b(d) = \begin{cases} 0, & \text{if } d < 0 \\ 1, & \text{if } d > D \\ r(d/D), & \text{otherwise.} \end{cases} \tag{3.1}$$

where D is chosen such that all points at a distance $d(\boldsymbol{X}) \leq D$ are completely inside the domain. The mapping $\boldsymbol{x} = \mathcal{G}(\boldsymbol{X}, t)$ is a blended combination of the undeformed domain and a rigidly displaced domain $\boldsymbol{Y}(\boldsymbol{X})$:

$$\boldsymbol{x} = b(d(\boldsymbol{x}))\boldsymbol{X} + (1 - b(d(\boldsymbol{x})))\boldsymbol{Y}(\boldsymbol{X}). \tag{3.2}$$

This expression ensures that all points inside C will be mapped according to the rigid motion, all the points at a distance D or larger from the circle will be unchanged, and all the points in-between will be mapped smoothly.

Mapping velocity and deformation gradient is obtained by differentiating Eqn. 3.2. Results using this approach were presented in ref. [1].

3.3 Radial Basis Function Approach

In this approach, the mapping is obtained by using a multivariate interpolation scheme based on radial basis functions (RBFs). RBFs are commonly used in fluid-structure interaction computations to transfer information between the structural and the aerodynamic mesh. Ref. [3] presents an approach to use RBFs as a mesh deformation technique and compares various RBFs and their influence on mesh quality and computation time.

The RBFs based method requires no grid connectivity information, which makes it very attractive for unstructured mesh movement applications. Ref. [4] shows that the quality of the deformed mesh is comparable to that obtained using any of the existing mesh movement techniques (spring analogy or PDE based approaches). In terms of computation required, the radial basis function approach requires an LU decomposition of the interpolation matrix of size $N_{Boundary\ Nodes} \times N_{Boundary\ Nodes}$. Once this is done, no further computations, other than matrix multiplications, are required during the simulation. In terms of memory requirements, the method is expensive as a dependence matrix, of size $N_{Boundary\ Nodes} \times N_{Nodes}$, is to be stored.

Table 3.1: Radial basis functions.

Name	Definition
Gaussian	$\phi(\|\mathbf{x}\|) = e^{-\alpha\|\mathbf{x}\|}$
Thin Plate Spline	$\phi(\|\mathbf{x}\|) = \|\mathbf{x}\|^2 ln\|\mathbf{x}\|$
Hardy's Multiquadric	$\phi(\|\mathbf{x}\|) = \sqrt{(c^2 + \|\mathbf{x}\|^2)}$
Hardy's Inverse Multiquadric	$\phi(\|\mathbf{x}\|) = \frac{1}{\sqrt{(c^2+\|\mathbf{x}\|^2)}}$
Wendland's C0	$\phi(\|\mathbf{x}\|) = (1 - \|\mathbf{x}\|)^2$
Wendland's C2	$\phi(\|\mathbf{x}\|) = (1 - \|\mathbf{x}\|)^4(4\|\mathbf{x}\| + 1)$
Wendland's C4	$\phi(\|\mathbf{x}\|) = (1 - \|\mathbf{x}\|)^6(35\|\mathbf{x}\|^2 + 18\|\mathbf{x}\| + 3)$
Wendland's C6	$\phi(\|\mathbf{x}\|) = (1 - \|\mathbf{x}\|)^8(32\|\mathbf{x}\|^3 + 25\|\mathbf{x}\|^2 + 8\|\mathbf{x}\| + 1)$
Euclid's Hat	$\phi(\|\mathbf{x}\|) = \pi((\frac{1}{12}\|\mathbf{x}\|^3) - r^2\|\mathbf{x}\| + (\frac{4}{3}r^3))$

3.3.1 Formulation

Given the displacements at the boundary nodes, the interpolation function, s, describing the displacement at an arbitrary point in the domain, can be written as,

$$s(\boldsymbol{X}) = \sum_{i=1}^{N_b} \alpha_i \phi(\|\boldsymbol{X} - \boldsymbol{X}_{b_i}\|) + p(\boldsymbol{X}), \tag{3.3}$$

where $\boldsymbol{X}_{b_i}$ are the boundary nodes at which the values are known, $p(\boldsymbol{X})$ is a polynomial, ϕ is the chosen radial basis function (Table 3.1) and $\|\cdot\|$ is the Euclidean length function. For the term $p(\boldsymbol{X})$, linear polynomials are chosen to recover simple translations and rotations [9]. The coefficients α_i and the polynomial p $(= \beta_0 + \beta_1\xi + \beta_2\eta)$ are determined by requiring the exact recovery of the boundary displacements,

$$\mathbf{d}_{b_j} = s(\boldsymbol{X}_{b_j}) = \sum_{i=1}^{N_b} \alpha_i \phi(\|\boldsymbol{X}_{b_j} - \boldsymbol{X}_{b_i}\|) + \beta_0 + \beta_1 \xi_{b_j} + \beta_2 \eta_{b_j}. \tag{3.4}$$

This system of equations is augmented by an additional requirement,

$$\sum_{i=1}^{N_b} \alpha_i q(\boldsymbol{X}) = 0, \tag{3.5}$$

for all polynomials q with a degree less than or equal to that of polynomial p. This side condition guarantees that translations and rotations are recovered exactly and also the total force and moment are conserved in the case of CFD-CSD coupling problems. From equations 3.4 and 3.5, we get

$$\left\{ \begin{array}{c} \mathbf{d}_b \\ 0 \end{array} \right\} = \underbrace{\left[\begin{array}{cc} M & P \\ P & 0 \end{array} \right]}_{\hat{M}} \left\{ \begin{array}{c} \alpha \\ \beta \end{array} \right\} \tag{3.6}$$

where M is the interpolation matrix,

$$M_{ij} = \phi(\|\boldsymbol{X}_{b_j} - \boldsymbol{X}_{b_i}\|), \quad 1 \leq i, j \leq N_b$$

and P is a $Nb \times 3$ matrix with row j given by $[1, \xi_{b_j}, \eta_{b_j}]$. We compute and store the LU factorization of $\hat{M}$, and use it to solve for α and β using forward and back substitutions.

Next, to obtain the nodal displacements, we rewrite Eqn. 3.3 as a matrix equation,

$$\begin{aligned} \Delta x &= \bar{M}^T \alpha^x + \bar{P}\beta^x, \\ \Delta y &= \bar{M}^T \alpha^y + \bar{P}\beta^y, \end{aligned} \tag{3.7}$$

where $\bar{M}$ is the dependence matrix,

$$\bar{M}_{ij} = \phi(\|\boldsymbol{X}_j - \boldsymbol{X}_{b_i}\|), \quad 1 \leq i \leq N_b, \quad 1 \leq j \leq N,$$

and $\bar{P}$ is a $N \times 3$ matrix with row j given by $[1, \xi_j, \eta_j]$. The dependence matrix $\bar{M}$ and $\bar{P}$ are also computed once and stored for subsequent computations.

Computation of Mesh Velocity and Deformation Gradient

The mesh velocities are obtained by differentiating Eqns. 3.6 and 3.11 to obtain,

$$\begin{Bmatrix} \dot{\mathbf{d}}_b \\ 0 \end{Bmatrix} = \begin{bmatrix} M & P \\ P & 0 \end{bmatrix} \begin{Bmatrix} \dot{\alpha} \\ \dot{\beta} \end{Bmatrix}, \tag{3.8}$$

and

$$\begin{aligned} \dot{x} &= \bar{M}^T \dot{\alpha}^x + \bar{P}\dot{\beta}^x, \\ \dot{y} &= \bar{M}^T \dot{\alpha}^y + \bar{P}\dot{\beta}^y, \end{aligned} \tag{3.9}$$

respectively. It should be noted that $\bar{M}$, $\bar{P}$, M and P do not change with respect to time, as they are always computed on the reference mesh. Hence, calculation of velocities require just additional matrix-vector products.

For the calculation of the deformation gradient, recall that the displacement at any point inside an element of the DG discretization can be written as a linear combination

of nodal displacements,

$$\Delta x = \sum_{i=1}^{N_p} \Delta x_i \bar{\phi}_i, \qquad \Delta y = \sum_{i=1}^{N_p} \Delta y_i \bar{\phi}_i \tag{3.10}$$

where Δx_i and Δy_i are the nodal displacements and $\bar{\phi}_i$ are the nodal basis functions used in the DG discretization. The new mesh positions x and y are given by,

$$x = \xi + \Delta x, \qquad y = \eta + \Delta y. \tag{3.11}$$

The deformation gradients are obtained by differentiating Eqns. 3.10 and 3.11,

$$\begin{aligned} x_\xi &= 1 + \sum_{i=1}^{N_p} \Delta x_i \bar{\phi}_{\xi_i}, \quad x_\eta = \sum_{i=1}^{N_p} \Delta x_i \bar{\phi}_{\eta_i}, \\ y_\xi &= \sum_{i=1}^{N_p} \Delta y_i \bar{\phi}_{\xi_i}, \qquad y_\eta = 1 + \sum_{i=1}^{N_p} \Delta y_i \bar{\phi}_{\eta_i}. \end{aligned} \tag{3.12}$$

An example of mesh deformation using RBF based approach, is shown in Figure 3-2, where a rectangular domain with a square and circular hole is deformed, such that the square and circular hole translate and rotate while the outer boundary is fixed. The simulation is performed using a gaussian RBF.

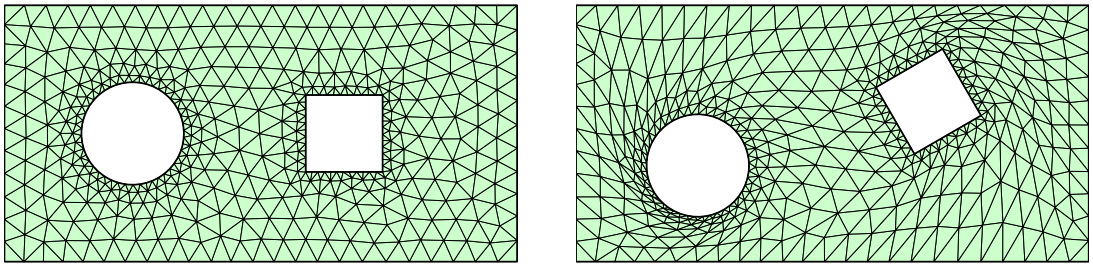

(a) Original Mesh.

(b) Deformed mesh, with the circle and square undergoing translation and rotation.

Figure 3-2: Mesh deformation using radial basis function based approach.

3.4 Linear Elasticity as a Mapping Technique

In the linear elasticity approach, the mesh is modelled as a continuum of elastic solid, characterized by the modulus of elasticity and Poisson's ratio, and the nodal movements are governed by the equations of linear elastodynamics.

In the present work, we use a viscoelastic material model, to attenuate the elastic waves generated due to the boundary motion.

3.4.1 Formulation

The equations of motion for linear elastodynamics can be written as,

$$\sigma_{ij,j} + F_i = \rho \partial_{tt} u_i. \tag{3.13}$$

For an isotropic, elastic solid, the stress-strain law (in the absence of thermal or nonmechanical effects) is given by,

$$\sigma_{ij} = \lambda \epsilon_{kk} \delta_{ij} + 2\mu \epsilon_{ij}, \tag{3.14}$$

where λ and μ are Lame's constants and the strain-displacement relations yield,

$$\epsilon_{ij} = \frac{1}{2}(u_{i,j} + u_{j,i}). \tag{3.15}$$

In the present approach, because of the high-order accurate spatial discretization, it is possible that the elastic waves generated could bounce back and forth between the boundaries and corrupt the solution. Hence, we propose to use a viscoelastic material instead of an elastic material, to dampen these waves. Using the Kelvin-Voigt model for viscoelastic materials, the stress-strain law becomes,

$$\sigma_{ij} = (\lambda \epsilon_{kk} + \hat{\lambda} \dot{\epsilon}_{kk}) \delta_{ij} + 2(\mu \epsilon_{ij} + \hat{\eta} \dot{\epsilon}_{ij}), \tag{3.16}$$

where λ, $\hat{\lambda}$, μ and $\hat{\eta}$ are Lame's constants. Writing equations 3.13 and 3.16 in a simplified form, we get

$$\frac{\partial}{\partial t}\begin{Bmatrix} \rho\dot{u} \\ \rho\dot{v} \end{Bmatrix} - \frac{\partial}{\partial x}\begin{Bmatrix} \sigma_x \\ \tau_{xy} \end{Bmatrix} - \frac{\partial}{\partial y}\begin{Bmatrix} \tau_{xy} \\ \sigma_y \end{Bmatrix} = \begin{Bmatrix} f(x,y) \\ g(x,y) \end{Bmatrix}, \tag{3.17}$$

and

$$\begin{Bmatrix} \sigma_x \\ \sigma_y \\ \tau_{xy} \end{Bmatrix} = \frac{E}{1-\nu^2}\begin{bmatrix} 1 & \nu & 0 \\ \nu & 1 & 0 \\ 0 & 0 & \frac{(1-\nu)}{2} \end{bmatrix}\begin{Bmatrix} \epsilon_x \\ \epsilon_y \\ \gamma_{xy} \end{Bmatrix} + \frac{\eta}{1-\nu^2}\begin{bmatrix} 1 & \nu & 0 \\ \nu & 1 & 0 \\ 0 & 0 & \frac{(1-\nu)}{2} \end{bmatrix}\begin{Bmatrix} \dot{\epsilon}_x \\ \dot{\epsilon}_y \\ \dot{\gamma}_{xy} \end{Bmatrix}, \tag{3.18}$$

respectively, where ν is the Poisson's ratio, E is the modulus of elasticity, ρ is the density of the material, η is the damping coefficient, $f(x,y)$ and $g(x,y)$ are the forcing functions.

Computation of Mesh Velocity and Deformation Gradient

The mesh velocity is obtained directly from the solution of Eq. 3.17. To compute the deformation gradient we augment our system of equations with two ODEs,

$$\frac{\partial}{\partial t}\begin{Bmatrix} \rho\dot{u} \\ \rho\dot{v} \\ u \\ v \end{Bmatrix} - \frac{\partial}{\partial x}\begin{Bmatrix} \sigma_x \\ \tau_{xy} \\ 0 \\ 0 \end{Bmatrix} - \frac{\partial}{\partial y}\begin{Bmatrix} \tau_{xy} \\ \sigma_y \\ 0 \\ 0 \end{Bmatrix} = \begin{Bmatrix} f(x,y) \\ g(x,y) \\ \dot{u} \\ \dot{v} \end{Bmatrix}. \tag{3.19}$$

This system of equations when solved with the discontinuous Galerkin method, (presented in next section), generates the deformation gradient as a part of the solution process. Alternatively, the deformation gradient can also be computed as described in section 3.3.1.

3.4.2 Numerical Solution

The linear elasticity equations are discretized using the compact discontinuous Galerkin (CDG) technique presented in Ref. [12]. The equations are written as a system of first order equations by introducing an additional variable $\boldsymbol{q}$,

$$\begin{aligned} \frac{\partial \boldsymbol{u}}{\partial t} - \nabla \cdot \boldsymbol{F}(\boldsymbol{q}) &= f \qquad && \text{in } \Omega, \\ \boldsymbol{q} &= \nabla \boldsymbol{u} \qquad && \text{in } \Omega, \\ \boldsymbol{u} &= g_D \qquad && \text{on } \partial\Omega_D, \end{aligned} \tag{3.20}$$

where $\boldsymbol{n}$ is the outward unit normal to the boundary of Ω and the vector $\boldsymbol{u}$ and fluxes $\boldsymbol{F}$ are defined according to equation 3.19.

Next, we introduce the '*broken*' DG spaces $\mathcal{V}^h$ and Σ^h associated with the triangulation $\mathcal{T}^h = \{K\}$ of V. In particular, $\mathcal{V}^h$ and Σ^h denote the spaces of functions whose restriction to each element K are polynomials of order $p \geq 1$.

Following [11], we consider DG formulations of the form: find $\boldsymbol{u}^h \in \mathcal{V}^h$ and $\boldsymbol{q}^h \in \Sigma^h$ such that for all $K \in \mathcal{T}^h$, we have,

$$\int_K \left.\frac{\partial \boldsymbol{u}^h}{\partial t}\right|_X \boldsymbol{V}\, dV - \int_K \boldsymbol{F}(\boldsymbol{q}^h) \cdot \boldsymbol{\nabla} \boldsymbol{V}\, dV - \int_{\partial K} \boldsymbol{V}(\hat{\boldsymbol{F}} \cdot \boldsymbol{N})\, dA = \int_K f \boldsymbol{V} dV \qquad \forall \boldsymbol{V} \in \mathcal{V}^h, \tag{3.21}$$

$$\int_K \boldsymbol{q}^h \boldsymbol{P}\, dV + \int_K \boldsymbol{u}^h \boldsymbol{\nabla} \cdot \boldsymbol{V}\, dV - \int_{\partial K} \hat{\boldsymbol{u}}^h (\boldsymbol{P} \cdot \boldsymbol{N})\, dA = 0 \qquad \forall \boldsymbol{P} \in \Sigma^h. \tag{3.22}$$

Here, the numerical fluxes $\hat{\boldsymbol{F}} \cdot \boldsymbol{N}$ and $\hat{\boldsymbol{u}}$ are approximations to $\boldsymbol{F} \cdot \boldsymbol{N}$ and to $\boldsymbol{u}$, respectively, on the boundary of the element K. The DG formulation is complete once we specify the numerical fluxes $\hat{\boldsymbol{F}} \cdot \boldsymbol{N}$ and $\hat{\boldsymbol{u}}$ in terms of $(\boldsymbol{u}^h)$ and $(\boldsymbol{q}^h)$ and the boundary conditions.

The numerical fluxes are viscous in nature and are chosen according to the compact discontinuous Galerkin (CDG) method [12]. This is a variant of the local discontinuous Galerkin (LDG) method [11], but has the advantage of being compact on general unstructured meshes.

Time integration is performed using implicit BDF2 scheme.

3.4.3 Results

We choose a tandem-foil system, (see figure 3-3), to evaluate the linear elasticity approach. In this particular case, the y-displacement of the forward foil is given by,

$$y_c(t) = A\sin(2\pi\omega t), \tag{3.23}$$

where $A = 1$ and $\omega = 0.25$, and the rear foil is stationary. The unstructured triangular mesh, shown in figure 3-3, consists of 3436 elements and polynomials of degree $p = 2$ are used within each element. We choose the following parameters for our problem, $E = 1700000$ N/m^2, $\rho = 1000$ kg/m^3, $\eta = 40$, and $\nu = 0.3$.

For this case, we observe degenerate elements for small displacements of the forward foil. Such behaviour was also reported in [7] and various fixes based on selective stiffening of the elements were proposed. Here we adopt the mesh stiffening based on the area of the element, i.e., smaller elements are made stiffer than the larger ones. To accomplish this, we choose the modulus of elasticity for an element as,

$$E = \frac{1700000}{\Delta}, \tag{3.24}$$

where Δ is the area of the element. This approach fixes the mesh degeneracy and yields a robust mesh movement strategy.

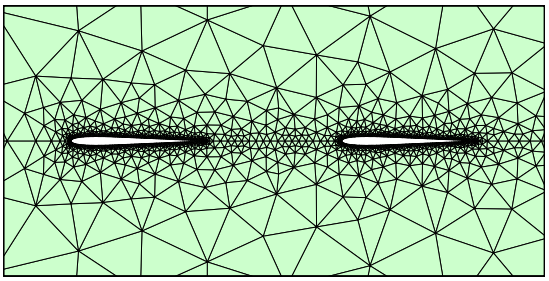

(a) Original mesh.

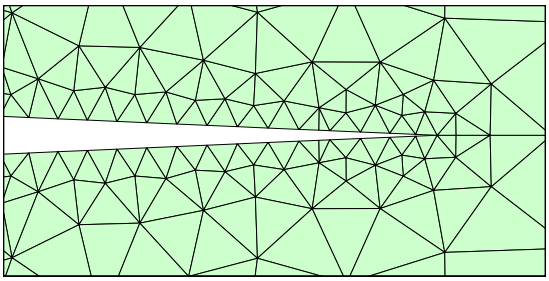

(b) Trailing edge of the oscillating foil in the original mesh.

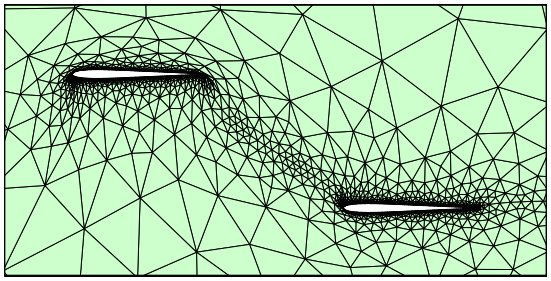

(c) Deformed mesh using constant modulus of elasticity.

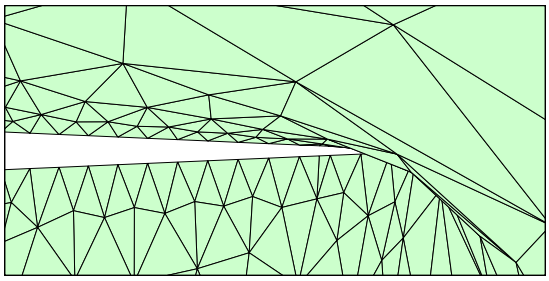

(d) Trailing edge with degenerate elements using constant modulus of elasticity.

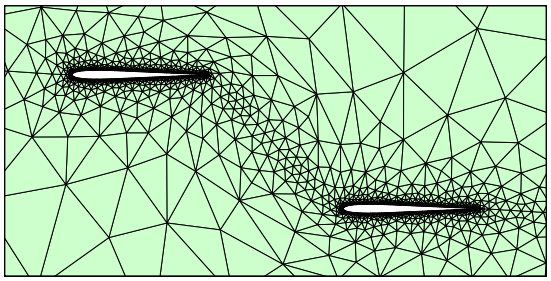

(e) Deformed mesh using variable modulus of elasticity.

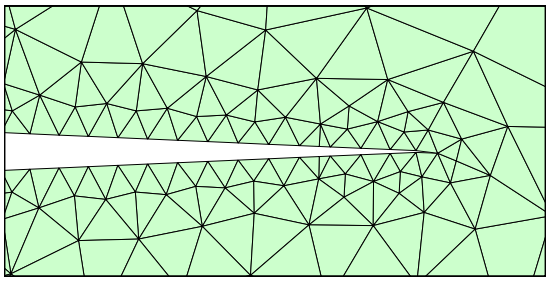

(f) Trailing edge of the oscillating foil in the deformed mesh using variable modulus of elasticity.

Figure 3-3: Mesh deformation using linear elasticity approach

Chapter 4

Examples

In this chapter, we solve a number of model problems to demonstrate the high-order accuracy of our scheme. Results are obtained using radial basis function and linear elasticity based mapping. Optimal convergence is shown in both the cases. A coupled ALE-linear elasticity approach is also presented in which the flow equations and the mesh motion equations are solved simultaneously.

4.1 ALE with Radial Basis Function based Mapping

In this section, results are presented for the solution of modified Navier-Stokes equations (Eqn. 2.12) and the geometric conservation law (Eqn. 2.13), with the radial basis function (RBF) based mapping. Gaussian RBF is used for all the studies.

4.1.1 Free Stream Preservation

For the present problem, we use a rectangular domain of size 20×15. We specify displacements at selected nodes in the interior domain. These displacements are

given by,

$$\left.\begin{aligned}\Delta x(\xi,\eta,t) &= \sqrt{2}\sin^2(\pi t/t_0)\sin(\pi r/2)\cos(\theta)\\ \Delta y(\xi,\eta,t) &= \sqrt{2}\sin^2(\pi t/t_0)\sin(\pi r/2)\sin(\theta)\end{aligned}\right\} \quad \text{if } 3 \le r \le 5, \tag{4.1}$$

where $r = \sqrt{(\xi-10)^2+\eta^2}$, $\theta = \tan^{-1}(\frac{\eta}{\xi-10})$ and $t_0 = \sqrt{10^2+5^2}$. The outer boundary nodes are fixed and the displacements for the remaining nodes are calculated using the RBF based approach. Note that at times $t = 0$ and $t = t_0$, the mapping is the identity mapping which makes solution initialization and comparison straightforward. Uniform freestream is used as the initial condition and we integrate in time until $t = 1.0$ using explicit Runge-Kutta method. It is observed that the L_2 norm of the errors are of the order of discretization errors. Hence, our scheme obeys the geometric conservation law and preserves freestream flow.

4.1.2 Euler Vortex

We demonstrate the high-order accuracy of our scheme by solving an inviscid model problem consisting of a compressible vortex on a rectangular domain [15, 16]. We use the same grid and time dependent mapping as in the previous example. The vortex is initially centered at (x_0, y_0) and is moving with the free-stream at an angle θ with respect to the x-axis. The analytic solution at (x, y, t) is given by,

$$\begin{aligned}
u &= u_\infty\left(\cos\theta - \frac{\epsilon((y-y_0)-\bar{v}t)}{2\pi r_c}\exp\left(\frac{f(x,y,t)}{2}\right)\right),\\
v &= u_\infty\left(\sin\theta + \frac{\epsilon((x-x_0)-\bar{u}t)}{2\pi r_c}\exp\left(\frac{f(x,y,t)}{2}\right)\right),\\
\rho &= \rho_\infty\left(1 - \frac{\epsilon^2(\gamma-1)M_\infty^2}{8\pi^2}\exp\left(f(x,y,t)\right)\right)^{\frac{1}{\gamma-1}},\\
p &= p_\infty\left(1 - \frac{\epsilon^2(\gamma-1)M_\infty^2}{8\pi^2}\exp\left(f(x,y,t)\right)\right)^{\frac{\gamma}{\gamma-1}},
\end{aligned} \tag{4.2}$$

where $f(x,y,t) = (1-((x-x_0)-\bar{u}t)^2-((y-y_0)-\bar{v}t)^2)/r_c^2$, M_∞ is the Mach number, $\gamma = c_p/c_v$, and u_∞, p_∞, ρ_∞ are free-stream velocity, pressure, and density. The Cartesian components of the free-stream velocity are $\bar{u} = u_\infty\cos\theta$ and $\bar{v} = u_\infty\sin\theta$.

The parameter ϵ measures the strength of the vortex and r_c is its size. The vortex is initially centered at $(x_0, y_0) = (5, 5)$ with respect to the lower-left corner. The Mach number is $M_\infty = 0.5$, the angle $\theta = \arctan 1/2$, and the vortex has the parameters $\epsilon = 0.3$ and $r_c = 1.5$. We use periodic boundary conditions and integrate until time $t_0 = \sqrt{10^2 + 5^2}$, when the vortex has moved a relative distance of $(10, 5)$.

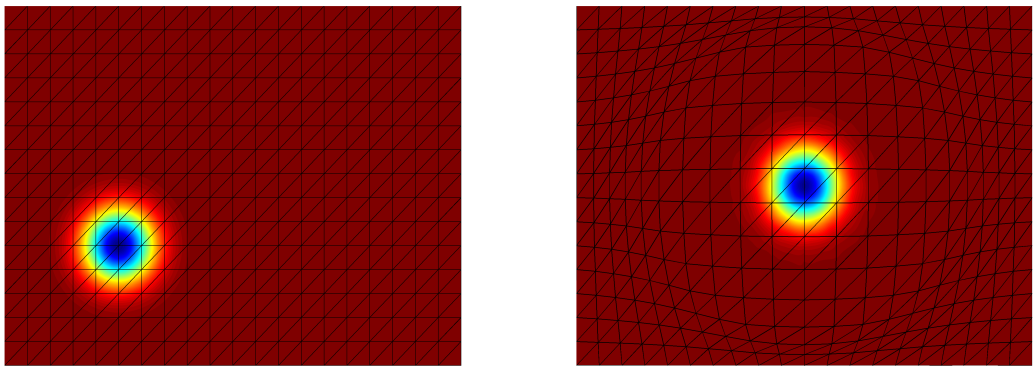

(a) Deformed mesh and solution, $t = 0$.

(b) Deformed mesh and solution, $t = (1/2)t_0$.

Figure 4-1: Mesh deformation and solution obtained by solving modified Navier-Stokes equations using RBF based mapping. The deformed mesh is shown for visualization, all the computations are performed on the reference mesh.

The solution and the deformed meshes at time $t = 0$ and $t = (1/2)t_0$ are shown in figure 4-1.

We solve, using explicit Runge-Kutta method, for different mesh sizes and polynomial orders using both the mapped and unmapped approaches. We obtain optimal convergence $O(h^{p+1})$, based on L_2 norm of the error, for both the schemes. The unmapped approach is more accurate, because the mapping leads to variations in the resolution of the vortex.

4.1.3 Oscillating Cylinder

In this example, we qualitatively compare the results for viscous flow around an oscillating cylinder using RBF based method and rigid mapping based approach. For the case of rigid mapping, the entire computational domain undergoes only translation

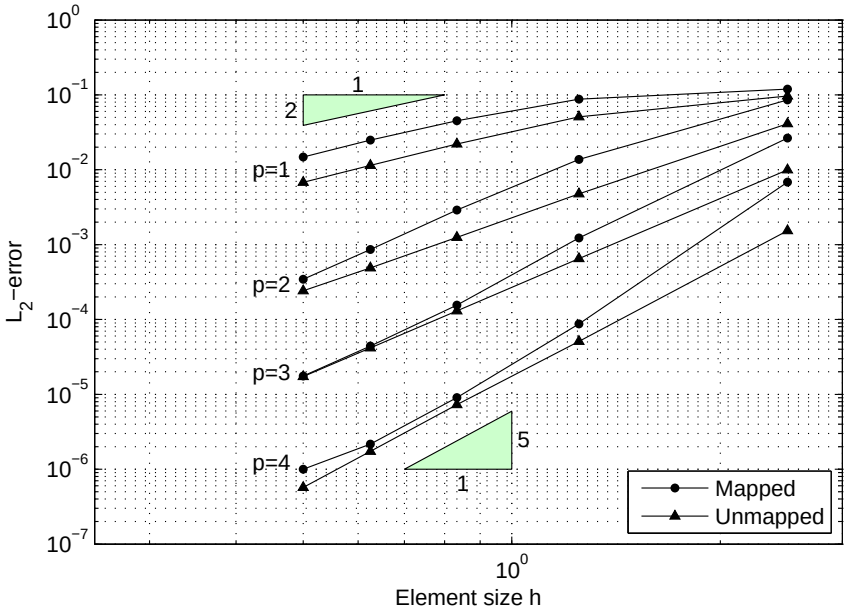

Figure 4-2: The convergence plots for mapped and unmapped schemes for the Euler vortex problem using radial basis function based approach.

and/or rotation, resulting in a mapping with $g = 1$. Hence, we do not need the GCL in this case.

In the present problem, the y-displacement of the cylinder is given by,

$$y_c(t) = A\sin(2\pi\omega t), \tag{4.3}$$

where $A = 4/3$ and $\omega = 0.1$. The Reynolds number with respect to the diameter is 400 and the Mach number is 0.2. Also, the unstructured mesh used has 1316 elements and we use polynomials of degree $p = 4$ within each element for our simulations. The meshes and solution using the two methods are shown in figure 4-3. The results obtained are remarkably similar after a considerably large time integration interval.

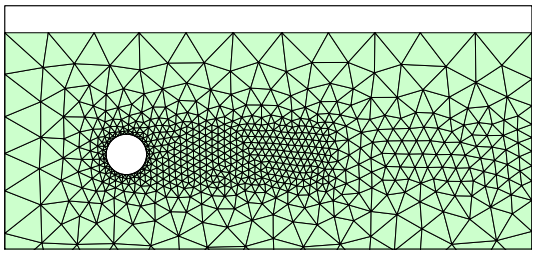

(a) Deformed mesh (rigid mapping).

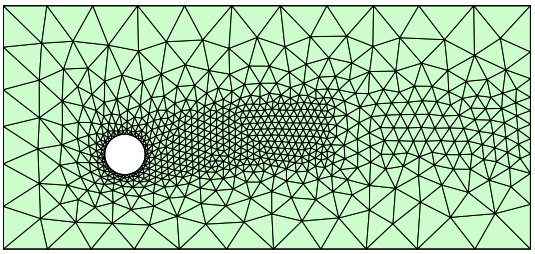

(b) Deformed mesh (RBF based mapping).

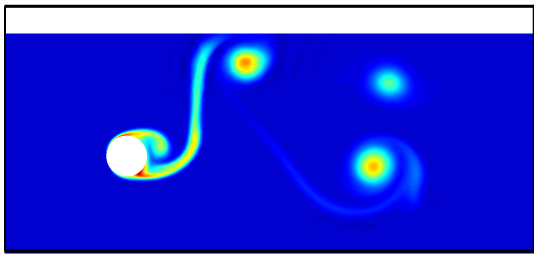

(c) Entropy, $t = 17.5$ (rigid mapping).

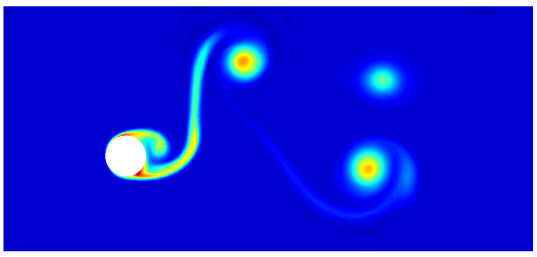

(d) Entropy, $t = 17.5$ (RBF based mapping).

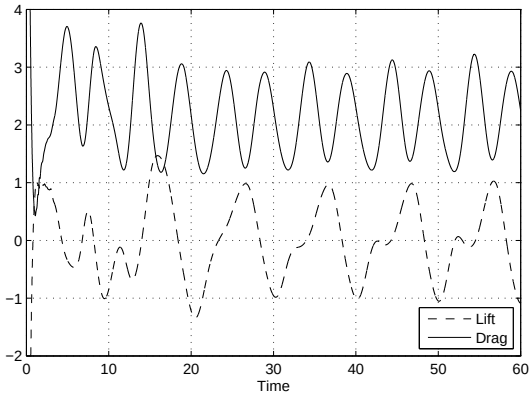

(e) Lift and drag coefficients (rigid mapping).

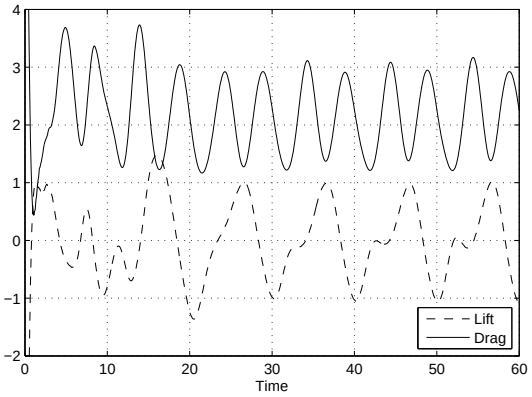

(f) Lift and drag coefficients (RBF based mapping).

Figure 4-3: Comparison of results obtained using rigid mapping and radial basis function(RBF) based mapping. The deformed mesh is shown for visualization only.

4.2 ALE with Linear Elasticity based Mapping

In this section, results are presented for the solution of modified Navier-Stokes equations (Eqn. 2.12) and the geometric conservation law (Eqn. 2.13), with the linear elasticity based mapping. The grid velocities and displacements are obtained by solving the linear elasticity equations (refer Eqn. 3.19) using discontinuous Galerkin approach and subsequently making the solution continuous at the element edges. This ensures that we obtain a continuous mapping as assumed in the ALE formulation. The deformation gradients are computed from the displacements using the method outlined in section 3.3.1.

4.2.1 Euler Vortex

For the present problem, we use a rectangular domain of size 20×15. Mesh motion is achieved by prescribing a forcing function in the interior of the domain,

$$\begin{aligned} f(\xi,\eta) &= 100000\,\mathrm{sgn}(\xi-10)\sin^2(2\pi t/t_0)\exp(-r^2/16), \\ g(\xi,\eta) &= 100000\,\mathrm{sgn}(\eta)\sin^2(4\pi t/t_0)\exp(-r^2/16), \end{aligned} \tag{4.4}$$

where $r = \sqrt{(\xi-10)^2+\eta^2)}$ and sgn is the signum function. A constant modulus of elasticity $E = 0.17GPa$ is used for all the simulations. The problem is initialized as described in section 4.1.2, We solve using periodic boundary conditions and integrate until time $t_0 = \sqrt{10^2+5^2}$. An implicit BDF2 method is used to solve for different mesh sizes and polynomial orders. We obtain optimal convergence $O(h^{p+1})$, based on L_2 norm of the error (Fig. 4-5).

4.2.2 Oscillating Cylinder

In this example, we compare the results for an oscillating cylinder obtained using linear elasticity approach with the rigid mapping approach. The results obtained show very good agreement and are shown in figure 4-6.

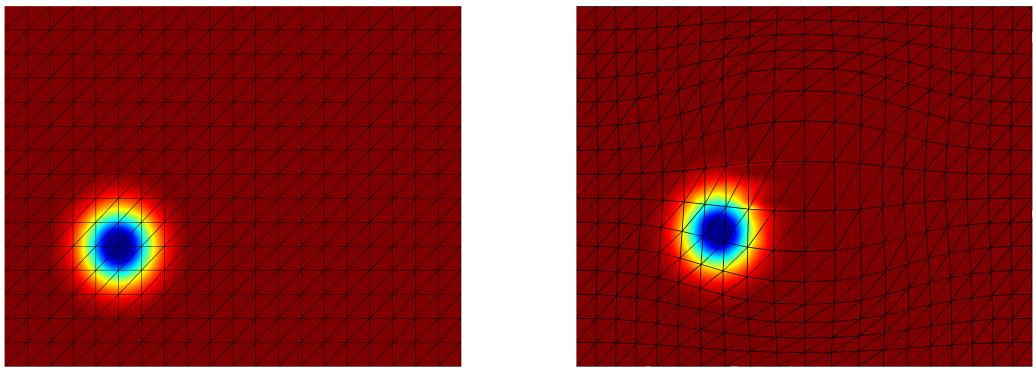

(a) Deformed mesh and solution, $t = 0$.

(b) Deformed mesh and solution, $t = (1/8)t_0$.

Figure 4-4: Mesh deformation and solution of the modified Navier-Stokes equations using linear elasticity based mapping approach. The deformed mesh is shown for visualization.

4.3 Coupled ALE-Linear Elasticity Formulation

4.3.1 Governing Equation

The coupled ALE-Linear elasticity approach combines the transformed Navier-Stokes equations along with the geometric conservation law, with the linear elasticity equations. By doing this we obtain a system of 9 equations, given by,

$$\frac{\partial}{\partial t}\begin{Bmatrix} \bar{g}g^{-1}\boldsymbol{U}_X \\ \bar{g} \\ \boldsymbol{v}_X \\ \boldsymbol{u} \end{Bmatrix} + \boldsymbol{\nabla}_X \cdot \begin{Bmatrix} \boldsymbol{F}_X \\ -g\boldsymbol{G}^{-1}\boldsymbol{v}_X \\ -\sigma_{\mathbf{ij}}/\rho \\ \mathbf{0} \end{Bmatrix} = \begin{Bmatrix} \mathbf{0} \\ 0 \\ \boldsymbol{f}(\xi,\eta) \\ \boldsymbol{v}_X \end{Bmatrix}, \tag{4.5}$$

where $\boldsymbol{U}_X$ is the vector of conserved variables in the reference domain, g is the jacobian, $\bar{g}$ is the correction to the jacobian, $\boldsymbol{G}$ is the deformation gradient, $\boldsymbol{v}_X$ are the mesh velocities, σ_{ij} are the stresses, ρ is the material density, $\boldsymbol{f}(\xi,\eta)$ are the forcing functions and $\boldsymbol{u}$ are the mesh displacements.

To obtain the DG formulation, we rewrite this system as a system of first order equations and discretize in the same way as shown in sections 2.3 and 3.4.2. The inviscid numerical fluxes are obtained using the Lax Friedrichs scheme and the viscous

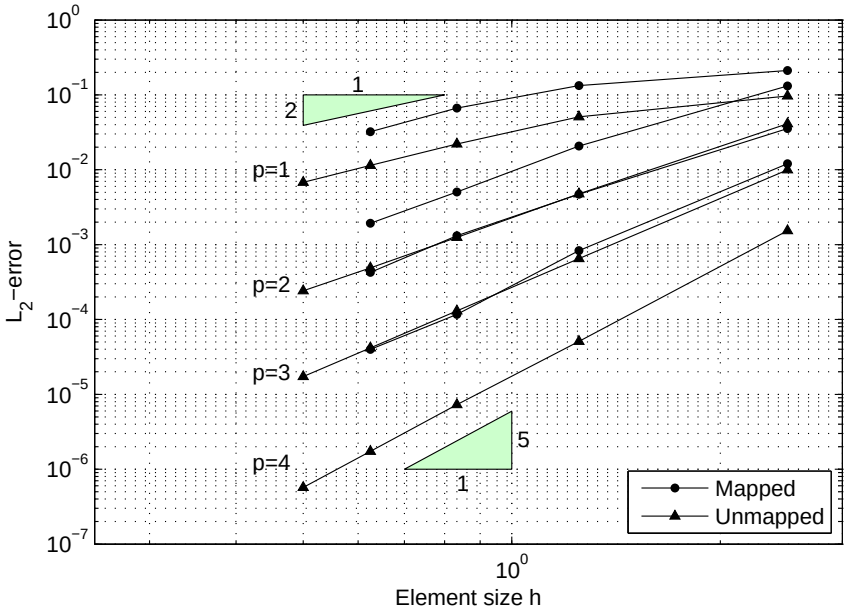

Figure 4-5: The convergence plots for mapped and unmapped schemes for the Euler vortex problem using linear elasticity approach.

fluxes are chosen using the CDG scheme.

4.3.2 Euler Vortex

Here also, the problem is initialized as described in section 4.1.2, mesh motion is achieved using the forcing function given by Eqn. 4.4. We solve using periodic boundary conditions and integrate until time $t_0 = \sqrt{10^2 + 5^2}$. An implicit BDF2 method is used to solve for different mesh sizes and polynomial orders. We obtain sub-optimal convergence $O(h^p)$, based on L_2 norm of the error (Fig. 4-8). This is because jumps are introduced in the mesh velocities and deformation gradient when solved using the discontinuous Galerkin approach.

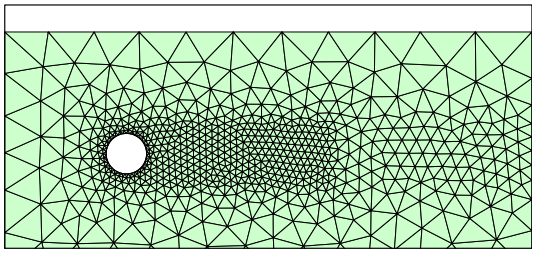

(a) Deformed mesh (rigid mapping).

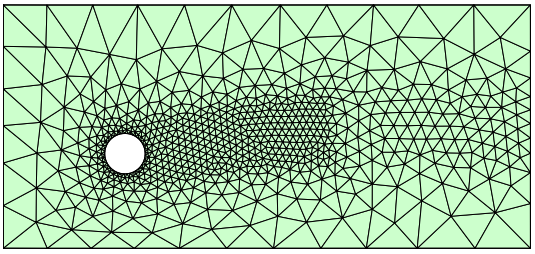

(b) Deformed mesh (linear elasticity based mapping).

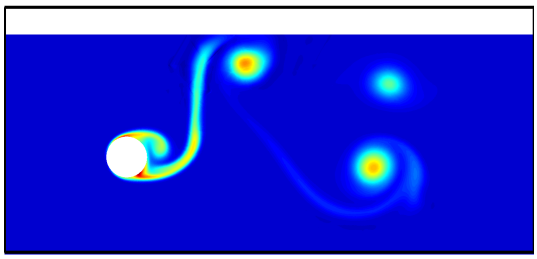

(c) Entropy, $t = 17.5$ (rigid mapping).

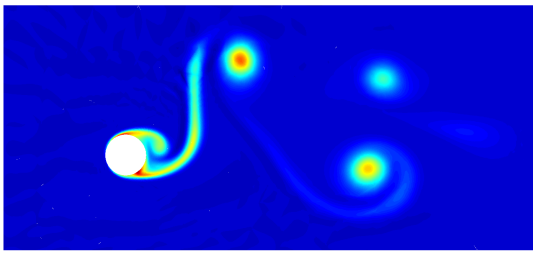

(d) Entropy, $t = 17.5$ (linear elasticity based mapping).

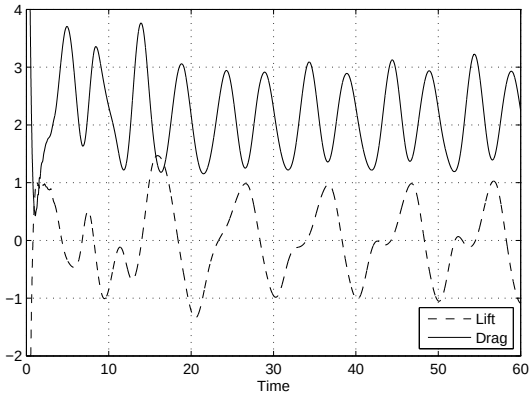

(e) Lift and drag coefficients (rigid mapping).

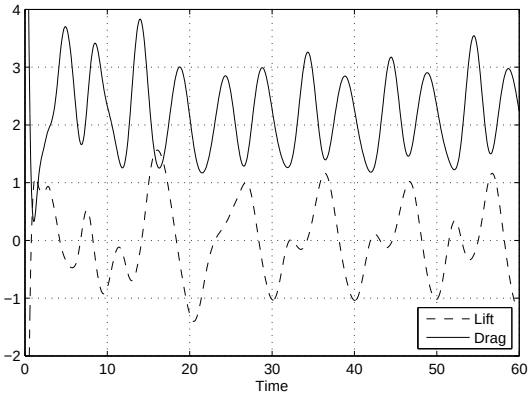

(f) Lift and drag coefficients (Linear elasticity based mapping).

Figure 4-6: Comparison of results obtained using rigid mapping ($p = 4$), and linear elasticity based mapping ($p = 3$).

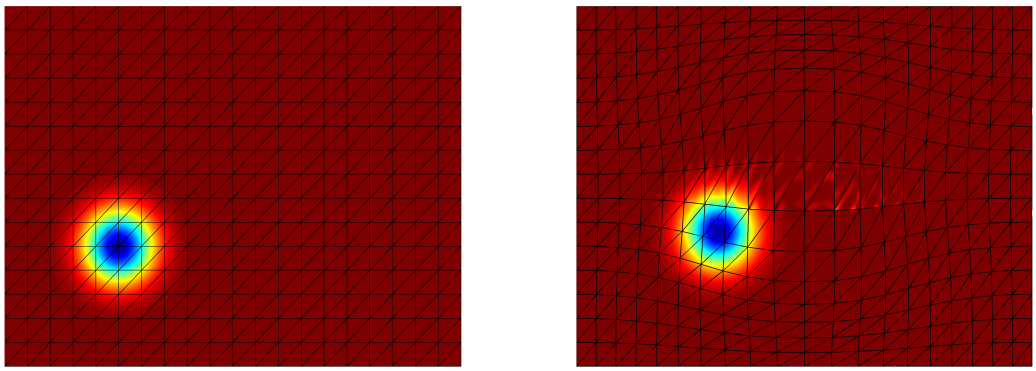

(a) Deformed mesh and solution, $t = 0$ (b) Deformed mesh and solution, $t = (1/8)t_0$

Figure 4-7: Mesh deformation and solution obtained by solving coupled ALE-linear elasticity equations. The deformed mesh is shown for visualization, all the computations are performed on the reference mesh.

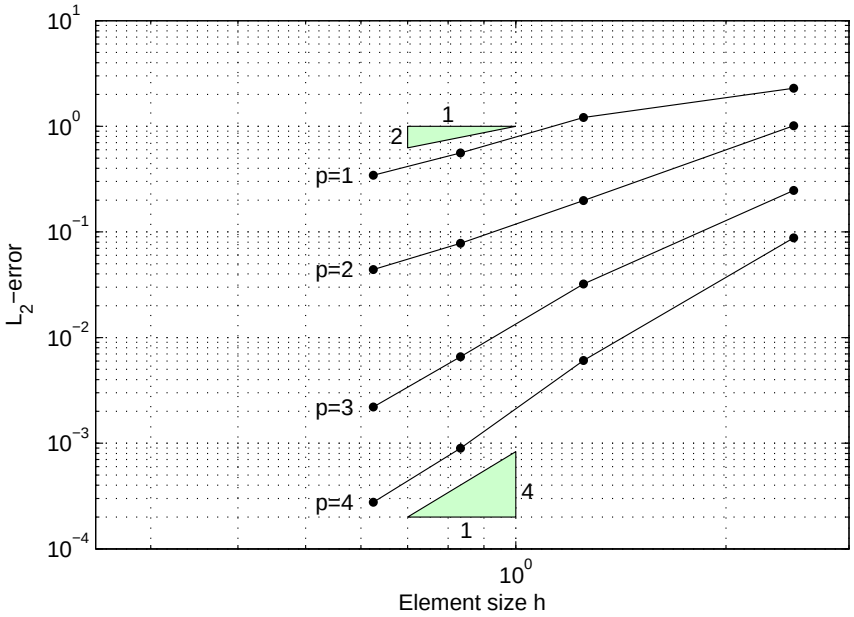

Figure 4-8: The convergence plots for mapped and unmapped schemes for the Euler vortex problem for the coupled ALE-linear elasticity formulation.

Chapter 5

Low Reynolds Number Flow around an Oscillating Cylinder

Flow around an oscillating circular cylinder is of interest to fluid dynamicists and offshore engineers. A large number of experimental and theoretical studies have been conducted, primarily to obtain the drag and inertia coefficients for different flow regimes. Tatsuno and Bearman [17] classified the flow regimes based on the following three parameters,

$$\begin{aligned} \text{Keulegan-Carpenter Number} \qquad & KC = \frac{U_m T}{D} = \frac{(\omega A)(2\pi/\omega)}{D} = \frac{2\pi A}{D}, \\ \text{Stokes' Parameter} \qquad & \beta = \frac{\rho D^2}{\mu T}, \\ \text{Reynolds Number} \qquad & Re = KC \times \beta = \frac{\rho U_m D}{\mu}, \end{aligned} \tag{5.1}$$

where μ is the coefficient of viscosity, ρ is the fluid velocity, T is the time period of oscillation, A is the amplitude of oscillation and ω is the oscillation frequency. In this chapter, we investigate various low Reynolds number flow regimes over an oscillating cylinder and compare the results obtained with those presented in the literature.

5.1 Theory

For a cylinder oscillating in a stationary fluid with a transverse motion, the inline force per unit length is a combination of the drag and inertia forces and is given by the Morison's equation [18],

$$F_1(t) = -\frac{1}{2}\rho D C_D \dot{x}|\dot{x}| - \frac{1}{4}\rho\pi D^2 C_I \ddot{x}, \tag{5.2}$$

where D is the diameter of the cylinder, ρ is the density of the fluid, C_D and C_I are the drag and added mass coefficients respectively. These coefficients are determined either experimentally or by numerical solution of the Navier-Stokes equations. Estimates are then made using method of least squares or Fourier analysis over a cycle [19]. Analytical expressions for C_D and C_I for large values of β were obtained by Stokes [20]. Wang [21] extended this analysis and derived the following expression,

$$\begin{aligned} C_D &= \frac{3\pi^3}{2KC}\left[(\pi\beta)^{-1/2} + (\pi\beta)^{-1} - \frac{1}{4}(\pi\beta)^{-3/2}\right], \\ C_I &= 2 + 4(\pi\beta)^{-1/2} + (\pi\beta)^{-3/2}, \end{aligned} \tag{5.3}$$

for $KC \ll 1, Re \times KC \ll 1$, and $\beta \ll 1$. The first two terms in these formulaes are same as those obtained by Stokes [20].

5.2 Numerical Simulation

For the present simulations we use an unstructured triangular mesh with 6400 elements and polynomial of degree p=3 within each element. We use the radial basis function based approach to obtain the mapping parameters. Also, implicit BDF2 scheme is used for time integration.

In the present work, we study three cases, corresponding to different flow regimes (refer table 5.1). Case 1 corresponds to a two dimensional flow in which two vortices are shed symmetrically every half cycle, case 2 is also two dimensional with secondary streaming and no flow separation and case 3 is three dimensional corresponding to

Table 5.1: Flow regimes under investigation.

	KC	Re
Case 1	11.0	81.4
Case 2	3.14	165.79
Case 3	6.0	210.0

irregular switching of flow convection direction (refs. [17], [22]).

The transverse displacements of the cylinder are given by,

$$\begin{aligned} x(t) &= -A\sin(\omega t), \\ \dot{x}(t) &= -A\omega\cos(\omega t) = -U_m\cos(\omega t), \end{aligned} \tag{5.4}$$

where A is the amplitude of oscillation and ω is the oscillation frequency.

5.3 Results

We compute the added mass and the drag coefficients using Fourier averaging [19],

$$\begin{aligned} C_I &= -\frac{2U_m T}{\pi^3 D}\int_0^{2\pi}\frac{F_1\sin(\theta)}{\rho U_m^2 D}d\theta, \\ C_D &= \frac{3}{4}\int_0^{2\pi}\frac{F_1\cos(\theta)}{\rho U_m^2 D}d\theta, \end{aligned} \tag{5.5}$$

where $\theta = \frac{2\pi t}{T}$.

The inline force computed shows very good agreement with results obtained using Morison's formula (see figure 5-1).

Values for drag and added mass coefficients for case 3 are given in refs. [22], and [23] and agree with those obtained in the present study (refer table 5.2).

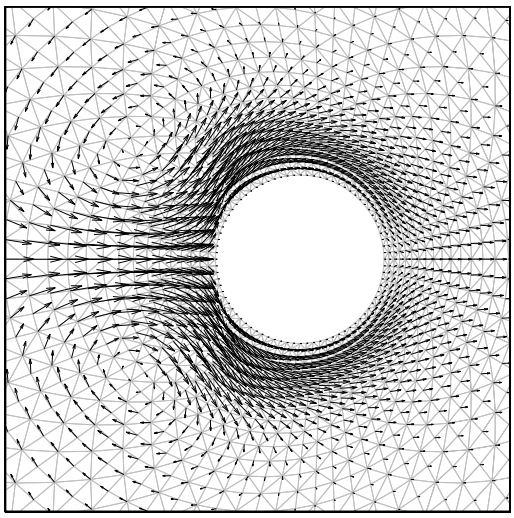

(a) Velocity field at t=250.2, Re=81.4, KC=11.0.

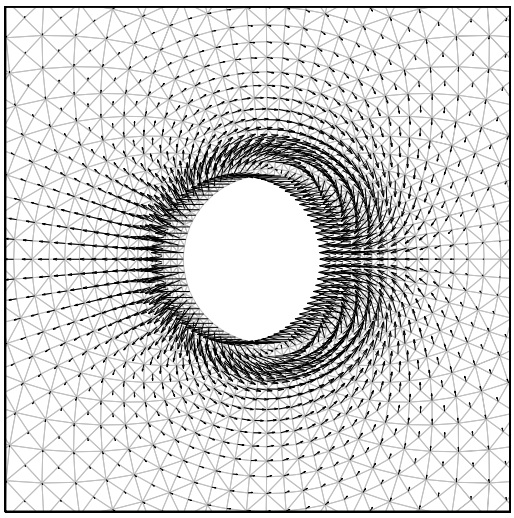

(b) Velocity field at t=59.64, Re=165.79, KC=3.14.

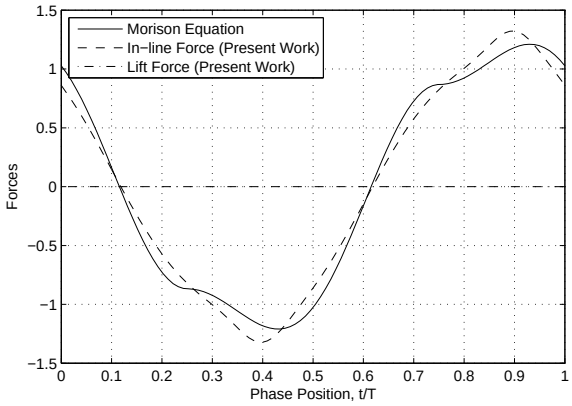

(c) In-line force over a cycle, Re=81.4, KC=11.0.

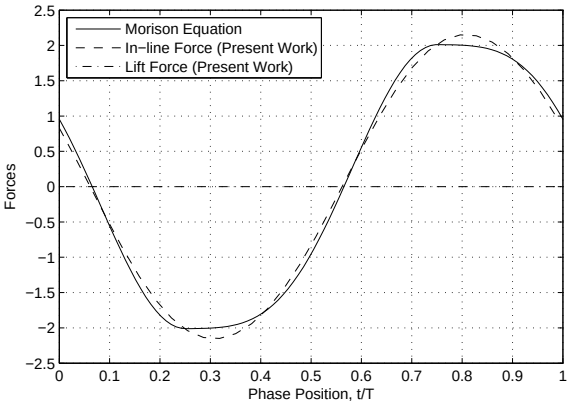

(d) In-line force over a cycle, Re=165.79, KC=3.14.

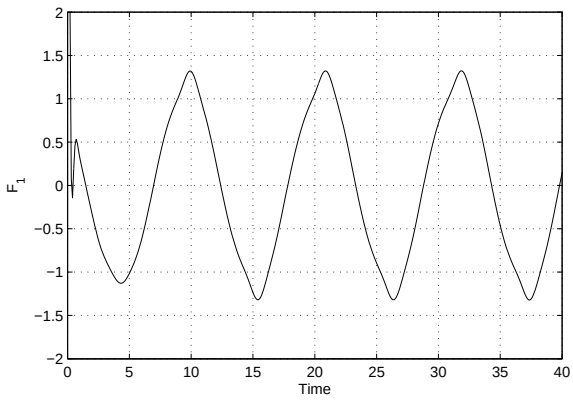

(e) Time history of in-line force, Re=81.4, KC=11.0.

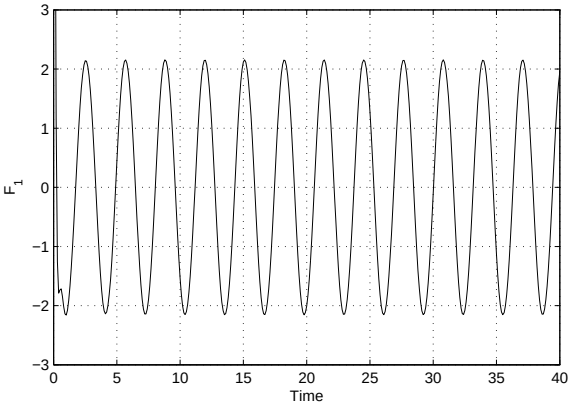

(f) Time history of in-line force, Re=165.79, KC=3.14.

Figure 5-1: Velocity field, in-line force and in-line force history for Case 1 (Re=81.4, KC=11.0) and Case 2 (Re=165.79, KC=3.14).

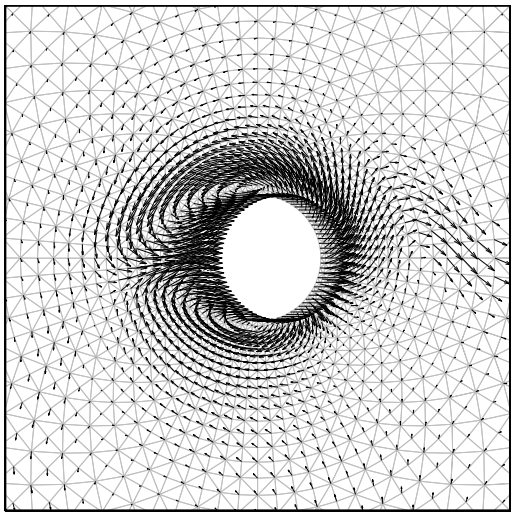

(a) Velocity field at t=465, Re=210, KC=6.0.

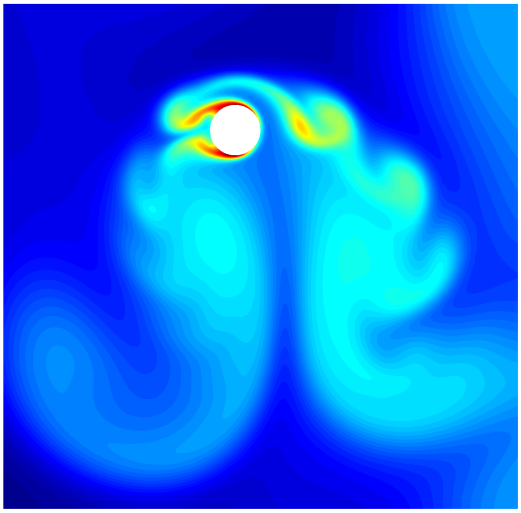

(b) Entropy, t=465, Re=210, KC=6.0.

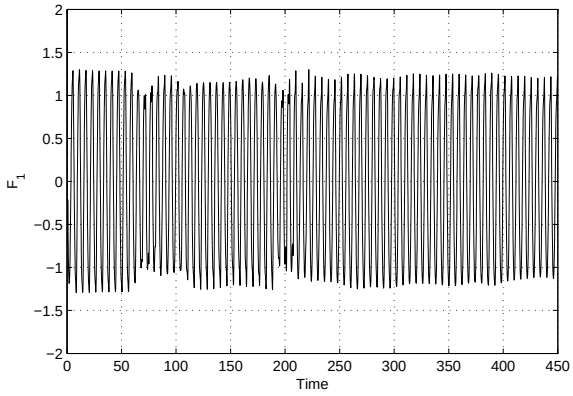

(c) Time history of in-line force, Re=210, KC=6.0.

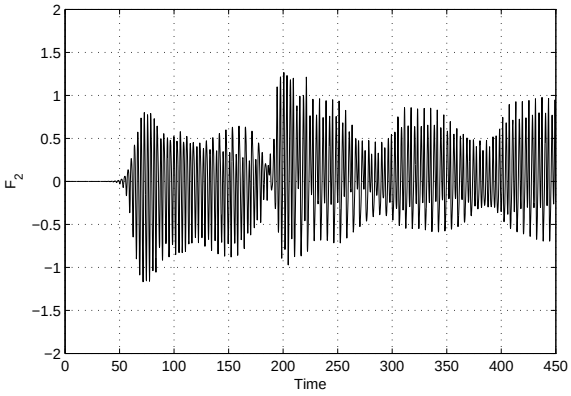

(d) Time history of lift force, Re=210, KC=6.0.

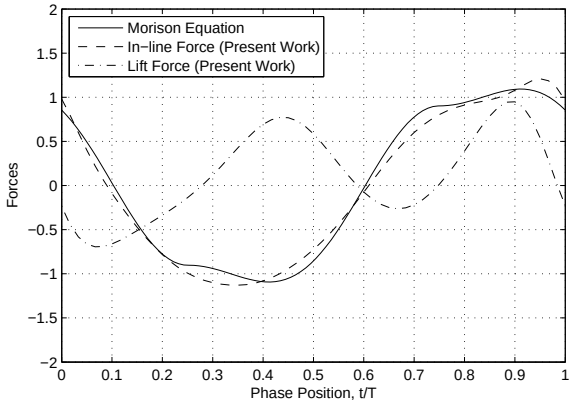

(e) In-line force over a cycle, Re=210, KC=6.0.

Figure 5-2: Velocity field, in-line force and in-line force history for Case 3 (Re=210, KC=6.0).

Table 5.2: Comparison of drag and added mass coefficients for KC=6 and Re=210.

	C_D	C_I
Present work	1.71	1.12
Viscous cell boundary element method [22]	1.75	1.14
Finite volume method [23]	1.73	1.17

Chapter 6

Conclusions

A coupled arbitrary Lagrangean Eulerian (ALE) approach to solve fluid-structure interaction using discontinuous Galerkin method is presented. Two mapping approaches based on radial basis function and linear elasticity are developed and coupled with the ALE formulation. The accuracy of the approach is demonstrated by showing freestream preservation, convection of a inviscid vortex and also comparison of results with those obtained using rigid mapping. A coupled ALE-linear elasticity approach is also presented.

Modified Navier-Stokes with radial basis functions based mapping was then used to investigate the low Reynolds number flow over an oscillating cylinder. Results were obtained and compared with those presented in the literature.

Appendix A

Compressible Navier-Stokes Equations

The two-dimensional compressible Navier-Stokes equations in cartesian coordinates without body forces and no external heat addition can be written as [24],

$$\frac{\partial \boldsymbol{U}}{\partial t} + \frac{\partial \boldsymbol{F}}{\partial x} + \frac{\partial \boldsymbol{G}}{\partial y} = 0, \tag{A.1}$$

where $\boldsymbol{U}, \boldsymbol{F}$ and $\boldsymbol{G}$ are given by,

$$\boldsymbol{U} = \begin{bmatrix} \rho \\ \rho u \\ \rho v \\ E \end{bmatrix}, \tag{A.2}$$

$$\boldsymbol{F} = \begin{bmatrix} \rho u \\ \rho u^2 + p - \tau_{xx} \\ \rho uv - \tau_{xy} \\ (E+p)u - u\tau_{xx} - v\tau_{xy} + q_x \end{bmatrix}, \tag{A.3}$$

$$\boldsymbol{G} = \begin{bmatrix} \rho v \\ \rho uv - \tau_{xy} \\ \rho v^2 + p - \tau_{yy} \\ (E+p)v - u\tau_{xy} - v\tau_{yy} + q_y \end{bmatrix}. \tag{A.4}$$

Also, for an ideal gas the equation of state becomes,

$$E = \frac{\rho}{\gamma - 1} + \frac{1}{2}\rho(u^2 + v^2). \tag{A.5}$$

The components of the shear-stress tensor and the heat-flux are given by,

$$\begin{aligned} \tau_{xx} &= \frac{2}{3}\mu\left(2\frac{\partial u}{\partial x} - \frac{\partial v}{\partial y}\right), \\ \tau_{yy} &= \frac{2}{3}\mu\left(2\frac{\partial v}{\partial y} - \frac{\partial u}{\partial x}\right), \\ \tau_{xy} &= \tau_{yx} = \mu\left(\frac{\partial u}{\partial y} + \frac{\partial v}{\partial x}\right), \\ q_x &= -k\frac{\partial T}{\partial x}, \\ q_y &= -k\frac{\partial T}{\partial y}, \end{aligned} \tag{A.6}$$

where μ is the coefficient of viscosity and k is the coefficient of thermal conductivity.

Bibliography

[1] P.-O. Persson, J. Bonet, and J. Peraire. Discontinuous Galerkin solution of the Navier-Stokes equations on deformable domains. *submitted to Computer Methods in Applied Mechanics and Engineering*, July 2008.

[2] Z. Yang and D. J. Mavriplis. Unstructured dynamic meshes with higher-order time integration schemes for the unsteady Navier-Stokes equations. *AIAA Paper*, 1222(2005):1, 2005.

[3] A. de Boer, M. S. Van der School, and H. Bijl. Mesh deformation based on radial basis function interpolation. *Computers and Structures*, 85:784–795, June 2007.

[4] C. B. Allen and T. C. S. Rendall. Unified approach to CFD-CSD interpolation and mesh motion using radial basis functions. *25th AIAA Applied Aerodynamics Conference, Miami, FL*, 2007.

[5] T.J. Baker and P.A. Cavallo. Dynamic adaptation for deforming tetrahedral meshes. *Computational Fluid Dynamics Conference, 14 th, Norfolk, VA*, pages 19–29, 1999.

[6] E. J. Nielsen and W. K. Anderson. Recent improvements in aerodynamic design optimization on unstructured meshes. *AIAA Journal*, 40(6):1155–1163, 2002.

[7] K. Stein, T. Tezduyar, and R. Benney. Mesh moving techniques for fluid-structure interactions with large displacements. *Journal of Applied Mechanics*, 70:58, 2003.

[8] R.P. Dwight. Robust mesh deformation using the linear elasticity equations. *Proceedings of the Fourth International Conference on Computational Fluid Dynamics (ICCFD 4), Ghent, Belgium*, 2006.

[9] A. Beckert and H. Wendland. Multivariate interpolation for fluid-structure-interaction problems using radial basis functions. *Aerospace Science and Technology*, 5(2):125–134, 2001.

[10] P.D. Thomas and C.K. Lombard. Geometric conservation law and its application to flow computations on moving grids. *AIAA Journal*, 17, 1979.

[11] B. Cockburn and C.-W. Shu. The local discontinuous Galerkin method for time-dependent convection-diffusion systems. *SIAM Journal on Numerical Analysis*, 35(6):2440–2463 (electronic), 1998.

[12] J. Peraire and P.-O. Persson. The compact discontinuous Galerkin (CDG) method for elliptic problems. *to appear in SIAM Journal on Scientific Computing*, 2008.

[13] P. L. Roe. Approximate Riemann solvers, parameter vectors, and difference schemes. *Journal of Computational Physics*, 43(2):357–372, 1981.

[14] J. Batina. Unsteady Euler airfoil solutions using unstructured dynamic meshes. *AIAA Journal*, 28(8):1381–1388, 1990.

[15] G. Erlebacher, M. Y. Hussaini, and C.-W. Shu. Interaction of a shock with a longitudinal vortex. *Journal of Fluid Mechanics*, 337:129–153, 1997.

[16] K. Mattsson, M. Svärd, M.H. Carpenter, and J. Nordström. High-order accurate computations for unsteady aerodynamics. *Computers & Fluids*, 36(3):636–649, 2007.

[17] M. Tatsuno and P. W. Bearman. A visual study of the flow around an oscillating circular cylinder at low Keulegan–Carpenter numbers and low Stokes numbers. *Journal of Fluid Mechanics Digital Archive*, 211:157–182, 2006.

[18] J. R. Morison, M. P. O'Brien, J. W. Johnson, and S. A. Schaaf. The force exerted by surface waves on piles. *Petroleum Transactions, AIME*, 189:149–154, 1950.

[19] T. Sarpkaya. Vortex shedding and resistance in harmonic flow about smooth and rough circular cylinders at high Reynolds numbers. 1976.

[20] G. G. Stokes. On the effect of the internal friction of fluids on the motion of pendulums. *Transactions of Cambridge Philosophical Society*, 9(8), 1851.

[21] C. Y. Wang. On high-frequency oscillatory viscous flows. *Journal of Fluid Mechanics*, 32:55–68, 1968.

[22] B. Uzunoglu, M. Tan, and W. G. Price. Low-Reynolds-number flow around an oscillating circular cylinder using a cell viscous boundary element method. *International Journal for Numerical Methods in Engineering*, 50:2317–2338, 2001.

[23] H. Dütsch, F. Durst, S. Becker, and H. Lienhart. Low-Reynolds-number flow around an oscillating circular cylinder at low Keulegan–Carpenter numbers. *Journal of Fluid Mechanics*, 360:249–271, 1998.

[24] D.A. Anderson, J.C. Tannehill, and R.H. Pletcher. Computational Fluid Mechanics and Heat Transfer. *McGraw-Hill, New York*, 1984.